

See discussions, stats, and author profiles for this publication at: <https://www.researchgate.net/publication/358797400>

Fault Source Model and Stress Changes of the 2021 Mw 7.4 Maduo Earthquake

Preprint · February 2022

CITATIONS

0

READS

234

7 authors, including:



Tai Liu

18 PUBLICATIONS 54 CITATIONS

SEE PROFILE



Yanfang Dong

China Earthquake Administration

40 PUBLICATIONS 261 CITATIONS

SEE PROFILE



Lize Chen

Institute of Earthquake Sciences, Beijing, China

10 PUBLICATIONS 45 CITATIONS

SEE PROFILE



Yueren Xu

Institute of Earthquake Forecasting, China Earthquake Administration

48 PUBLICATIONS 453 CITATIONS

SEE PROFILE

Some of the authors of this publication are also working on these related projects:



National Natural Science Foundation of China (grant 41502204) [View project](#)



National Natural Science Foundation of China (grant 42072248) [View project](#)

Fault Source Model and Stress Changes of the 2021 M_w 7.4 Maduo Earthquake, China, Constrained by InSAR and GPS Measurements

Shunying Hong^{*1}, Mian Liu², Tai Liu¹, Yanfang Dong¹, Lize Chen¹, Guojie Meng¹, and Yueren Xu¹

ABSTRACT

On 22 May 2021, an M_w 7.4 earthquake struck Maduo, China, within the eastern Bayan Har block of the Tibetan plateau. The eastward-extruding Bayan Har block is marked by active seismicity along its boundary faults, including the 2008 M_w 7.9 Wenchuan earthquake, but large earthquakes within the block are relatively rare. Thus, the Maduo earthquake could provide useful information about crustal deformation of the Tibetan plateau. Early reports, shortly after the earthquake, have suggested a sinistral strike-slip fault rupture, but the fault geometry and slip distribution vary in these models due to the limited observational constraints. Here, we reconstructed a model of fault geometry and coseismic slip using Interferometric Synthetic Aperture Radar and Global Positioning System data. A non-planar fault model was constructed based on pixel-offset images and the optimized dip angle. The along-strike variation of the dip angle is small, so a single optimized dip is used. Our results suggest that the Maduo earthquake ruptured ~ 156 km on a northwest-striking major fault that dips 78° , and ~ 24 km on a minor southeast-striking fault that dips 64° . Most fault slip occurred above 15 km depth, and released a moment of $\sim 1.65 \times 10^{20}$ N·m. Using the resolved fault source model, we calculated the change of coulomb failure stress in the region and on the neighboring faults. The Maduo earthquake highlighted intrablock deformation in the Tibetan plateau whereas numerous lithospheric blocks extrude along major strike-slip faults.

KEY POINTS

- InSAR and GPS data are jointly inverted for the fault source model of the 2021 Maduo, China, earthquake.
- The Maduo earthquake ruptured a ~ 156 km main fault and a ~ 24 km secondary fault.
- The Maduo earthquake increased stress on its neighboring faults within the Bayan Har block.

Supplemental Material

INTRODUCTION

On 22 May 2021, a magnitude M_w 7.4 earthquake struck Maduo (98.34° E, 34.59° N) in the Qinghai province, China, with a focal depth of approximately 17 km. This was the largest earthquake in mainland China since the devastating M_w 7.9 Wenchuan earthquake in 2008 and the first $M_w \geq 7.0$ earthquake inside eastern Bayan Har block since 1976 (see [Data and Resources](#)) (Fig. 1).

The Bayan Har block is an active block of the Tibetan plateau that has been extruding eastward during the late Cenozoic ([Zhang et al., 2005](#)). It is bounded by the sinistral East Kunlun

fault to the north, the sinistral Yushu–Ganzi and Xianshuihe faults to the south, and the transpressional Longmenshan fault to the east. These boundary faults are seismically active ([Deng et al., 2010](#)), hosting a series of $M_w \geq 6.5$ earthquakes since 1976 (Fig. 1), including the 1976 M_w 6.7 Songpan earthquake ([Jones et al., 1984](#); [Yang et al., 2021](#)), the 2001 M_w 8.1 Kunlun earthquake ([Lasserre et al., 2005](#)), the 2008 M_w 7.9 Wenchuan earthquake ([Shen et al., 2009](#)), and the 2011 M_w 6.9 Yushu earthquake ([Li et al., 2011](#)). In contrast, large earthquakes within the Bayan Har block have been relatively rare. The 2021 M_w 7.4 Maduo earthquake occurred inside the Bayan Har block, on the Maduo segment of the Jianguo fault

1. Institute of Earthquake Forecasting, China Earthquake Administration, Beijing, China, <https://orcid.org/0000-0002-6259-1323> (SH); <https://orcid.org/0000-0002-4057-8435> (TL); <https://orcid.org/0000-0001-7490-924X> (YD); <https://orcid.org/0000-0002-6584-0380> (GM); <https://orcid.org/0000-0001-7342-2210> (YX); 2. Department of Geological Sciences, University of Missouri, Columbia, Missouri, U.S.A.

*Corresponding author: hongshunying@ief.ac.cn

Cite this article as Hong, S., M. Liu, T. Liu, Y. Dong, L. Chen, G. Meng, and Y. Xu (2022). Fault Source Model and Stress Changes of the 2021 M_w 7.4 Maduo Earthquake, China, Constrained by InSAR and GPS Measurements, *Bull. Seismol. Soc. Am.* **XX**, 1–13, doi: [10.1785/0120210250](https://doi.org/10.1785/0120210250)

© Seismological Society of America

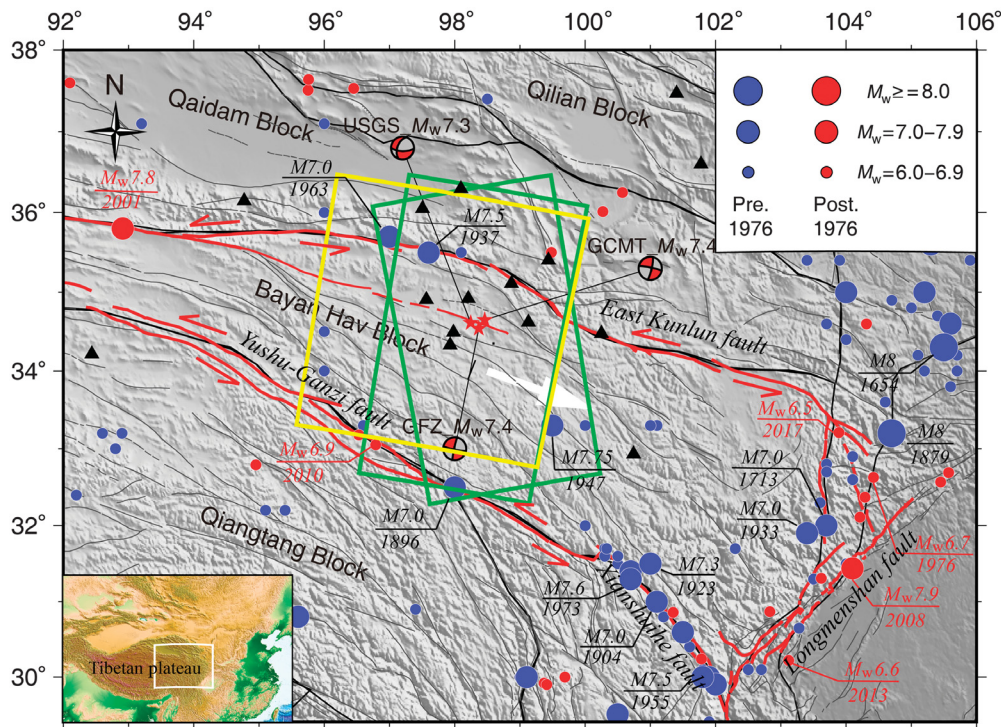


Figure 1. Map of topographic relief, earthquakes, and major faults for the 2021 Maduo epicenters (red stars) and surrounding regions. Focal mechanism solutions for the Maduo earthquake are from U.S. Geological Survey (USGS), Global Centroid Moment Tensor (Global CMT), and German Research Centre for Geosciences (GFZ), respectively. Red dots are $M_w \geq 6.0$ earthquakes from Global CMT since 1976. Blue dots are $M_w \geq 6.0$ earthquakes from the China Earthquake Networks Center (CENC) (see [Data and Resources](#)) before 1976. Rectangles are footprints of Interferometric Synthetic Aperture Radar (InSAR) measurements (green for S1A and S1D, and yellow for A2D in Table S1). Black triangles are the Global Positioning System (GPS) sites from [Li, Ding, et al. \(2021\)](#) used in the inversion of slip distribution. Lower-left inset shows the location of the main map.

([Li Z.-M. et al., 2021](#); [Wang et al., 2021](#)), which is poorly mapped, and its kinematics were almost unknown prior to this earthquake.

The 2021 Maduo earthquake thus provides an opportunity to study the internal structure and kinematics of the Bayan Har block and seismicity of the region. The focal mechanism solutions show that the earthquake resulted from a sinistral strike-slip rupture (Table 1). However, the fault geometry parameters are controversial. A northwest-striking fault that dips to the north is suggested by the Global Centroid Moment Tensor (Global CMT) solution. A southeast-striking fault that dips to the south is suggested by the solutions from the German Research Centre for Geosciences (GFZ) and the U.S. Geological Survey (USGS) (see [Data and Resources](#)). In addition, the rake angle from the USGS solution is $\sim 40^\circ$, contrasting to that from the GFZ (-3°) and the Global CMT (-9°). Furthermore, early studies, shortly after the earthquake, have considerable discrepancies in the fault parameters and/or slip models. A northwest-striking ($\sim 278.5^\circ$) fault with a dip angle of $\sim 64.4^\circ$ is derived from the Global Positioning System (GPS) coseismic offsets ([Li, Ding, et al., 2021](#)), whereas a nearly vertical fault plane is suggested by

the relocated aftershocks ([Wang et al., 2021](#)). A multisegments planar fault is inferred from the Interferometric Synthetic Aperture Radar (InSAR) deformation fields ([Chen et al., 2021](#); [Zhao et al., 2021](#)). Recently, a complex curved fault model with variable dip angle inferred from relocated aftershocks is also provided ([He et al., 2021](#)). The discrepancies of the fault-slip models contributed to variations in the coulomb failure stress (CFS) change on the surrounding faults ([He et al., 2021](#); [Li, Huang, et al., 2021](#)). These inconsistencies are mainly due to the limited observational constraints shortly after the earthquake, the simplified fault source models used for the inversions, and/or the uncertainties of aftershocks positions and their spatial relationship with fault plane.

In this study, we used the Sentinel-1A/B and Advanced Land Observation Satellite (ALOS) PALSAR-2 data to retrieve the coseismic deformation field in multiple Synthetic

Aperture Radar (SAR) viewing geometries. Using the coseismic InSAR deformation fields and horizontal GPS data, we first refined the source model with a nonplanar fault geometry using the SAR pixel-offset images. The dip angle and its along-strike variation are analyzed and optimized for the fault model. Then, the InSAR and GPS data were jointly inverted for the slip distribution. Finally, we used the optimal fault-slip model to calculate the CFS changes (Δ CFS) on the neighboring faults and within the Bayan Har block to explore the triggering effects on aftershocks and the impact on regional seismicity.

INSAR MEASUREMENT OF COSEISMIC DISPLACEMENT

InSAR measurement

We processed InSAR measurements with Single Look Complex data in Interferometric Wide swath model from the Sentinel-1A/1B and normal ScanSAR mode from ALOS PALSAR-2 satellite platforms (Table S1, available in the supplemental material to this article), respectively. The Sentinel-1A/1B satellite operates at the C-band with a radar wavelength about 5.6 cm. The ALOS PALSAR-2 operates at the L-band

TABLE 1

Parameters of the Source Model

Source	Top Fault Center							Depth (km)	Slip (m)	Mo ($\times 10^{20}$ N·m)	M_w	
	X (°)	Y (°)	Z (km)	Length (km)	Width (km)	Strike (°)	Dip (°)					Rake (°)
F1	-	-	-	177 (~156 rupture)	30	281.92 ^A	78	-1.30 ^A \pm 0.4	0.96 ^A \pm 0.01, 4.07 ^M \pm 0.04	4.40 ^{MS}	1.65	7.42
F2	-	-	-	30 (~24 rupture)	30	100.24 ^A	64	13.55 ^A \pm 1.2	0.49 ^A \pm 0.02, 2.46 ^M \pm 0.06	1.35 ^{MS}	-	-
Wang et al. (2021)	98.398 ^C	34.652 ^C	7.6 ^C	~170	-	~285	~90	-	-	-	-	M_s 7.4
Li Z. et al. (2021)	-	-	-	180	30	278.5	64.4	-10.9	4.2 ^M	-	1.85	7.45
Li Z.-M. et al. (2021)	-	-	-	160	-	Northwest-southeast	-	-	1-2	-	-	-
Liu et al. (2021)	-	-	-	-	~18	~102.1 A	90	-	~6 ^M	-	1.8	7.44
Chen et al. (2021)	Five segments	-	-	-	-	-	70~85	-	~5 ^M	~8 ^{MS}	1.45	7.41
Zhao et al. (2021)	Five segments	-	-	-	-	-	75~85	-	~6 ^M	~6-8 ^{MS}	-	7.38
He et al. (2021)	Nonplanar fault model with variable dip angles	-	-	-	-	-	-	-	4.2 ^M	-	1.80	7.4
USGS	98.251 ^C	34.598 ^C	23.5 ^C	-	-	92	67	-40	-	-	1.306	7.34
Global CMT	98.46 ^C	34.65 ^C	12.0 ^C	-	-	200	53	-151	-	-	1.71	7.4
GFZ	98.26 ^C	34.57 ^C	15.0 ^C	-	-	13	81	-173	-	-	1.40	7.4
						282	83	-9	-	-		
						102	84	-3	-	-		
						192	86	-174	-	-		

F1 and F2 are, respectively, the nonplanar main rupture and a second rupture from this study. Model of Wang et al. (2021) is from the relocated mainshock and aftershocks; Li Z.-M. et al. (2021) is a model from field investigation; Li, Ding, et al. (2021) is a model from the GNSS alone; Liu et al. (2021), Chen et al. (2021), and Zhao et al. (2021) are models from InSAR observation alone; He et al. (2021) is a model from InSAR and aftershocks. USGS, Global CMT, and GFZ are the focal mechanism solutions by seismic waveforms. The superscript C denotes the epicenter; the superscript A represents the average value; the superscript M represents the maximum, and the superscript MS represents the maximal slip. GFZ, German Research Centre for Geosciences; Global CMT, Global Centroid Moment Tensor; GNSS, Global Navigation Satellite Systems; InSAR, Interferometric Synthetic Aperture Radar; USGS, U.S. Geological Survey.

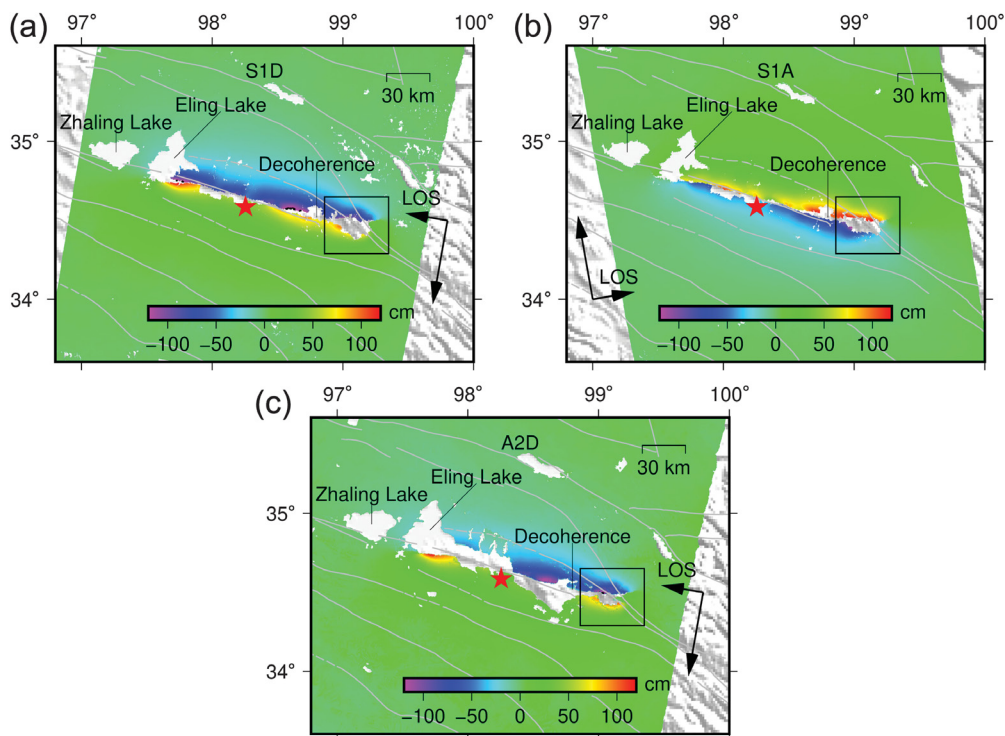


Figure 2. Coseismic deformation fields of the 2021 Maduo earthquake measured by InSAR tracks (a) S1D, (b) S1A, and (c) A2D, respectively. Positive values represent movement in line of sight (LOS) direction toward the Synthetic Aperture Radar (SAR) satellite platform; negative values indicate motion in the opposite direction. White areas are where measurements are missing due to decoherence caused by excessive deformation gradient or water coverage. The black box is the near-field region of F2; deformation in this area was masked for constraining the dip angle of F1. See [Optimal Dip Angles](#) section for discussion.

with a radar wavelength about 24.2 cm. The coseismic interferogram and/or its deformation field of the Sentinel-1 ascending orbit, descending orbit, and the ALOS-2 descending orbit is, respectively, referred to as S1A, S1D, and A2D in this study (Table S1).

With sparse vegetation and relatively flat terrain, the Maduo area has favorable conditions for maintaining interference coherence. We adopted the “two-pass D-InSAR processing” approach to extract deformational signals. The InSAR Scientific Computing Environment (ISCE) (Rosen *et al.*, 2012) was used to generate interferograms of the three interference pairs (Table S1). Precise orbit data for S1A and S1D were used to reduce potential orbit errors. The digital elevation model from the Shuttle Radar Topography Mission with a spatial resolution of ~ 30 m (Farr *et al.*, 2007) was used to remove the topographic phase contribution to the interferograms. Ionospheric contaminations are insignificant for the C-band because of its relatively shorter wavelength but are not negligible for the InSAR measurement with a long wavelength L- or P-band (Gray *et al.*, 2000). Therefore, extra ionospheric error correction was done for the A2D data operated at the L-band (Liang and Fielding, 2017; Liang *et al.*, 2018). The interferograms were then unwrapped with a branch cut algorithm

(Goldstein *et al.*, 1988), to avoid possible trend error of phase unwrapping for a deformation field with large-scale surface rupture.

Coseismic deformation and downsampling

The geocoded coseismic deformation field in line of sight (LOS) direction from the S1A, S1D, and A2D tracks is shown in Figure 2. The coseismic deformation is localized along a northwest–southeast rupture zone. A pattern of diametrically opposite motion is measured by the ascending orbits (Fig. 2a,c) and descending orbits (Fig. 2b), indicating that the coseismic displacement of the Maduo earthquake is dominated by horizontal movement, rather than vertical offset. This is consistent with the 3D coseismic deformation field derived by Liu *et al.* (2021) and Chen *et al.* (2021), and with the focal mechanism solutions from the Global CMT and GFZ that indi-

cate a sinistral strike slip (Table 1). Furthermore, the roughly symmetrical InSAR displacement across the rupture zone indicates a steep fault rupture.

The coseismic deformation fields were downsampled with the Kite software (Marius *et al.*, 2017). The unwrapped phases of S1A, S1D, and A2D from the ISCE were geocoded, rereferenced and converted into displacement in meters. A quadtree method (Jónsson *et al.*, 2002) was used to downsample the coseismic deformation field with a variance threshold of 0.02. The minimum and maximum dimension of the quadtree tile was set to 0.02° and 0.30° , respectively. The downsampling reduced the number of measurement points from over 10 million to 2394 for S1A, 2241 for S1D, and 1724 for A2D. This allows for efficient inversion calculations while preserving the near-field deformation characteristics. The uncertainties within the InSAR data are not estimated during the downsample, and unique weight for the three InSAR deformation fields is used in this study.

FAULT SOURCE MODEL

In this section, we used the InSAR data to construct a nonplanar fault model with an optimized dip angle and then jointly inverted the InSAR and GPS data to solve for slip distribution on the fault.

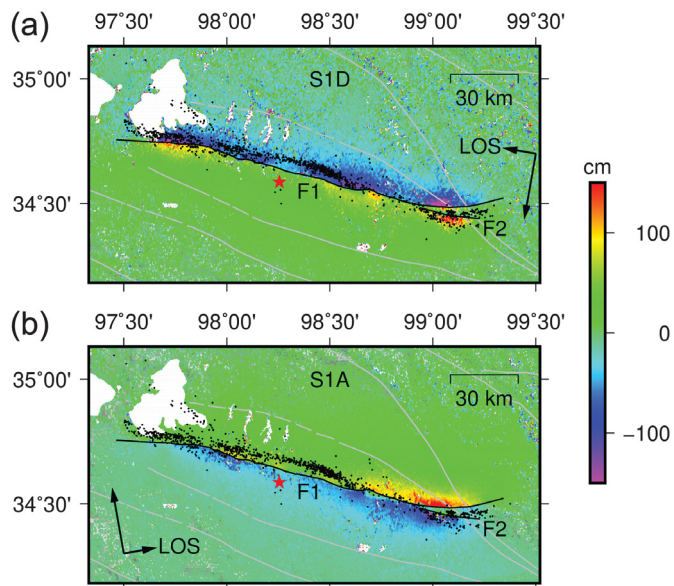


Figure 3. Range Pixel offsets calculated by the autoRIFT method for the Sentinel-1 (a) descending orbit (S1D) and (b) ascending orbit (S1A). Black lines are the constructed major fault (F1) and secondary fault (F2). Black dots are the relocated aftershocks (Wang *et al.*, 2021). Positive values represent movement toward the SAR satellite platform in the LOS direction; negative values mean the opposite motion.

Fault surface trace

The first step for constructing the fault model is to determine the surface rupture trace; we identified the trace using SAR pixel offsets. We used the Autonomous Repeat Image Feature Tracking (autoRIFT) method (Gardner *et al.*, 2018; Lei *et al.*, 2021) to extract the SAR pixel offsets from the S1A and S1D data. The autoRIFT algorithm calculates pixel displacements in the range and azimuth between two SAR or optical images with a nested grid design, sparse then dense combinative searching strategy, and disparity filtering technique (Lei *et al.*, 2021). The results (Fig. 3) show a fault trace composed of a main fault segment (F1) and an eastern branch fault (F2), generally consistent with field studies (Li Z.-M. *et al.*, 2021) and relocated aftershocks (Wang *et al.*, 2021).

The accuracy of the pixel offsets is related to the pixel size and pixel registration accuracy, which is usually 1/50th \sim 1/30th of a pixel size (Casu *et al.*, 2011; Lei *et al.*, 2021), lower than that of the InSAR measurement. Therefore, we only use the pixel offsets to determine the fault trace in the surface and do not use them to infer the fault dip and slip distribution.

Optimal dip angles

The nearly symmetric surface motion across the fault (Fig. 2a, b) indicates steep and roughly constant fault dip. We used surface motion along profiles across the fault strike to analyze dip variation (Fig. S1a,b), similar to the approach of Jolivet *et al.* (2014). We found the dip angle variation along the main fault

(F1) is $<5^\circ$ (Fig. S1c), which is difficult to distinguish by the InSAR data and/or relocated aftershocks. Therefore, we chose to use a single dip angle for the rupture model. More discussion is provided in the [Fault dip angle](#) section.

We used the downsampled InSAR coseismic displacements of S1A, S1D, and A2D to constrain the dip angles, assuming a constant dip for the F1 and F2, respectively. The relocated aftershocks are distributed at 0–25 km depth (Wang *et al.*, 2021). Therefore, the width of our model fault is set to be 30 km in the dip direction for both F1 and F2, as in previous studies (He *et al.*, 2021; Li, Ding, *et al.*, 2021). The F1 and F2 are about 177 km and 30 km long, respectively (Fig. 3), and were initially discretized into 590 and 100 patches, each with a size of 3×3 km. The Crust2.0 model (Bassin *et al.*, 2000) was used to compute the Green's functions.

The fault dip angle for F1 and F2 was optimized one after another, and both north- and south-dipping are explored. We first masked out the deformation fields in the near field of F2 (area shown in Fig. 2) and used the remaining deformation field to constrain the dip of F1. This is to avoid displacement disturbance from F2. The dip of F1 was sampled from 50° to 90° , with a step of 1° . Then, the slip distribution of F1 were batch inverted using the Steepest Descent Method (SDM) (Wang *et al.*, 2013). The optimal F1 dipping angle is 78° in northeast-dipping (i.e., northwest-striking), as indicated by the minimum misfit between the simulated displacement and the masked InSAR measurements (Fig. 4a,b).

With the F1 optimal dip angle, we then used the masked area (shown in Fig. 2) to constrain the dip angle of F2. Varying F2 dip angle with a step of 1° , the slip distribution of F1 and F2 were batch inverted, and the misfit in the masked area were calculated to determine the optimal dip angle of F2, which is estimated to be 64° in southwest-dipping (i.e., south-east-striking) (Fig. 4c,d).

Slip-distribution model

With the optimized fault geometry, slip distribution was then estimated by joint inversion of the InSAR and horizontal GPS data (Li, Ding, *et al.*, 2021). The GPS vertical displacement was not used because of its large uncertainty. The results vary with the smoothing factor and the weight ratio of GPS to InSAR. The optimal smoothing factor for stress drop distribution was set to 0.05, determined by the trade-off curve method (Fig. S2a), and the optimal weight ratio of GPS to InSAR was set to 40, determined by the trade-off between the normalized root mean square residual of InSAR and that of GPS (Fig. S2b). Using these optimal values, the slip distribution was resolved (Fig. 5). For comparison, we also inverted the slip distribution using only the GPS data as well as the combination of GPS and Sentinel-1 data (Fig. S3). The addition of InSAR data significantly enhances the resolution of the slip distribution.

The coseismic fault slip on F1 was distributed over a length of \sim 156 km, mainly above 15 km depth (Fig. 5). Three slip

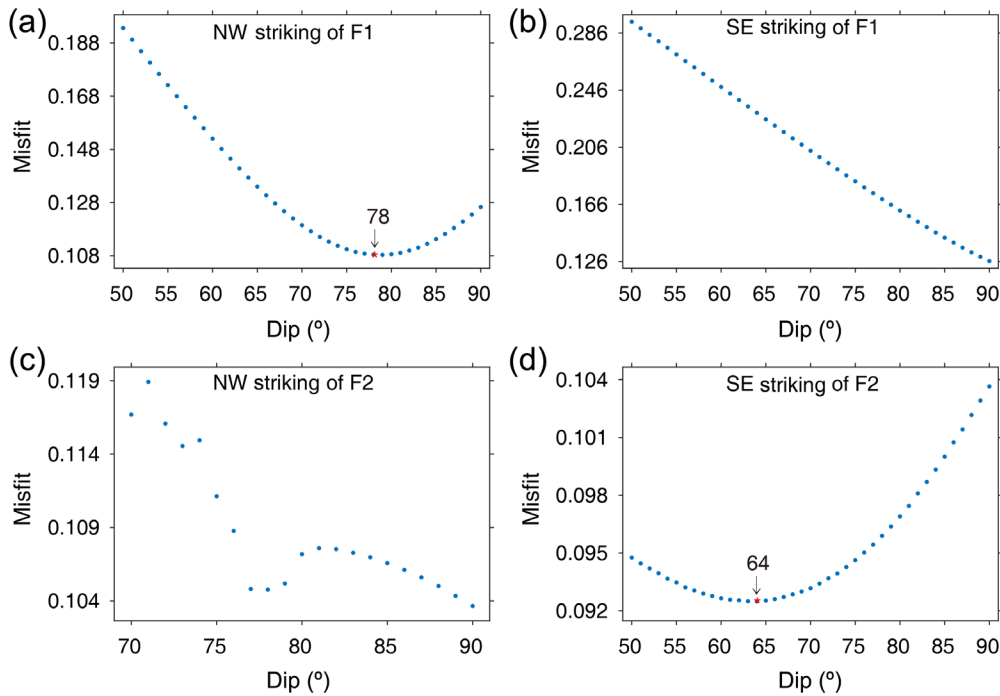


Figure 4. Optimization of fault dip angle based on misfits of InSAR-measured displacement and model predictions assuming varies dip angles. (a,b) Misfit of a northwest-striking F1 (a) and a southeast-striking F1 (b), derived from the InSAR deformation fields with the near-field region to F2 masked off (area shown in Fig. 2). (c,d) Same but for the secondary rupture plane F2, assuming a northwest-striking (c) or a southeast-striking (d), respectively, constrained only by the near-field InSAR displacements around F2. The color version of this figure is available only in the electronic edition.

centers are found at a depth range of 1–10 km, within the recoverable depth range as indicated by the checkerboard test (Fig. S4 and Text S1). The maximum slip is 4.07 m, which occurred around 97.74 E in the western segment of F1, at a depth of 4.4 km. The average rake angle is about -1.3° (Table 1), indicating a dominantly sinistral strike-slip motion. The slip distribution on fault F2 is shallower and lesser than on F1, and the slip occurs along a length of ~ 24 km. The ruptures of F1 and F2 have reached the surface in most places, consistent with the field observation (Li Z.-M. *et al.*, 2021). The total seismic moment release from the derived slip distribution was 1.65×10^{20} N·m (taking the shear modulus to be 30 GPa), equivalent to a magnitude M_w 7.42 earthquake.

The relocated aftershocks (Wang *et al.*, 2021) are also shown in Figure 5. Most aftershocks occurred where coseismic slip is low, and many occurred deeper (>15 km) than the main rupture zone, where stress is likely not fully released by the mainshock. Most area in the shallow zone (0–15 km) lacked aftershocks, indicating a relatively complete rupture. In a 3D view from east to west, F1 and F2 essentially pass through the concentration zone of the relocated aftershocks (Fig. 5c), comparable to the nearly vertical fault plane inferred solely from the relocated aftershocks (He *et al.*, 2021; Wang *et al.*, 2021). Some aftershocks extended to the north from the

western end of F1, but they are not associated with additional rupture that is either manifested in the deformation fields (Fig. 3) or observed in the field (Li Z.-M. *et al.*, 2021).

Uncertainty of the slip

The uncertainty of the slip distribution could be estimated by the integration of SDM and Monte Carlo (MC) method (Parsons *et al.*, 2006; Feng and Li, 2010). We generated 100 groups of InSAR measurement data with noise for the S1A, S1D, and A2D using the MC method. The anisotropic noises were synthetically produced through the full Variance–Covariance Matrix of the signals in the far field, assuming there the InSAR signals stemmed mainly from noises. Using the InSAR data and GPS constraints, we performed 100 inversions for slip distribution. The results were analyzed statistically to calcu-

late the standard deviation (uncertainty) of slip distribution (Fig. 6c,d and Table 1). The slip uncertainty (Fig. 6c,d) by the data noise was quietly small (<0.1 m).

The uncertainties from the smoothing factor and weight ratio of GPS to InSAR were also estimated (Fig. 6e–h). The smoothing factor was sampled at equal intervals between 0.025 and 0.750, and the weight ratio was also equidistantly sampled from 20 to 60. Then, we solved the slip distribution in batches and calculated their standard deviation. The smoothing factor could cause more uncertainties than the weight ratio of GPS to InSAR and data noises (Fig. 6e–h).

In general, the slip uncertainties are relatively low in comparison to the slip itself. The modeled slip distribution fits the observational data well, as judged from the inversion residuals. Figure 7 shows the comparison of the InSAR measured ground displacement with that simulated using the optimal fault-slip model. The root mean square error (RMSE) of S1D, S1A, and A2D is 4.8 cm, 4.7 cm, and 4.9 cm, respectively. This fault source model also predicts ground horizontal motion that is close to the horizontal GPS motions (Fig. 8), with a much smaller RMSE.

CFS CHANGE

Using the optimal fault source model (Fig. 5), we calculated the Δ CFS on the epicentral region and on the neighboring faults

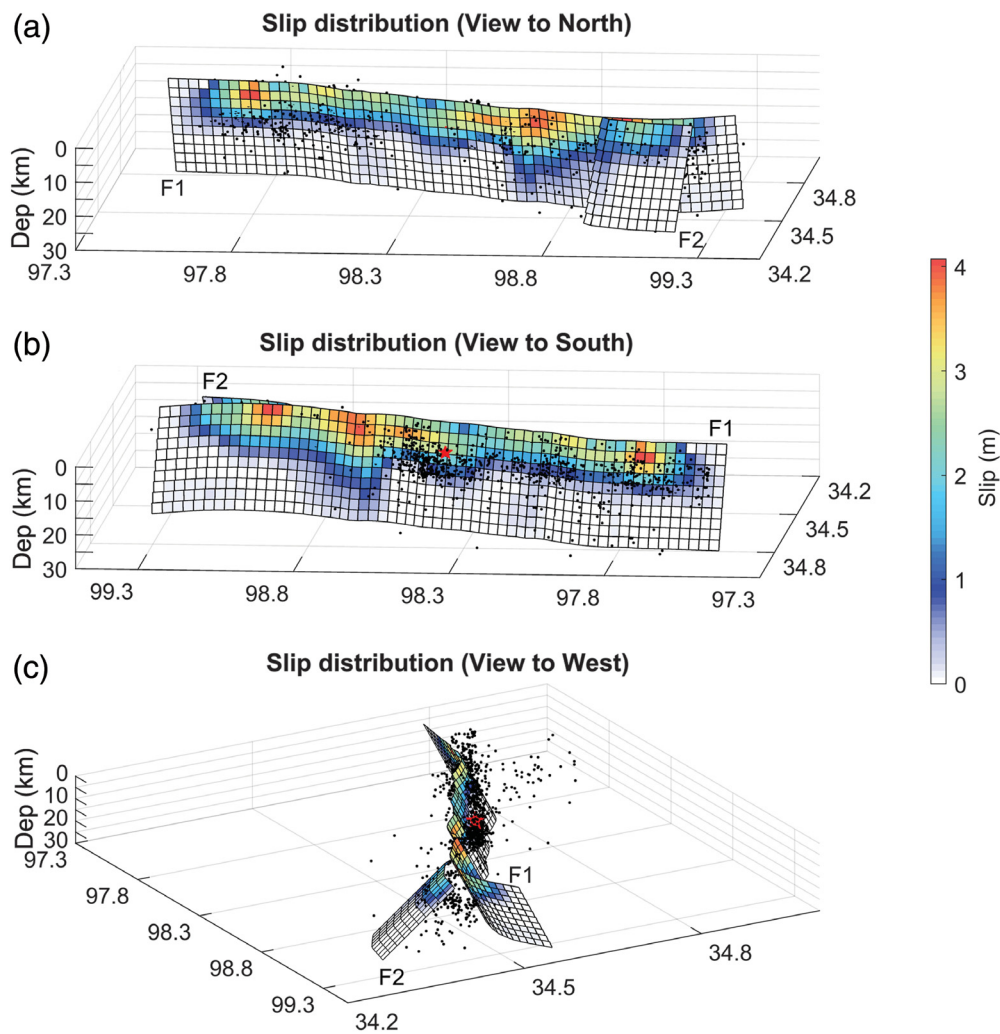


Figure 5. Fault-slip distribution (color contours) and relocated aftershocks (black dots) in the 3D coordinates. (a) View from south to north; (b) view from north to south; (c) view from east to west. F1 is the main rupture, striking northwest and dipping northeast (78°); F2 is the minor rupture, striking southeast and dipping southwest (64°). The relocated aftershocks and the mainshock (red star) are from Wang *et al.* (2021). The uncertainty of horizontal and vertical location for the relocated aftershocks is ~ 0.5 km and ~ 1 km, respectively (Wang *et al.*, 2021).

(Fig. 9) using the PSCMP and PSGRN code (Wang *et al.*, 2006). The Δ CFS on a receiver fault can be estimated by the change of shear stress, normal stress, and friction coefficient (Text S2). A rheologically stratified crust model was constructed based on previous studies (Wang *et al.*, 2017; Li, Huang, *et al.*, 2021); it is listed in Table S2.

Figure 9a shows the calculated coseismic Δ CFS at a depth of 10 km for the optimal planes, assuming the same parameters for all receiver faults as those of the mainshock rupture. The Δ CFS is up to ± 0.04 MPa in the epicentral region. In the vicinity of the rupture, the Δ CFS results are unreliable, because the finite strain there is unsuitable for the dislocation model based on linear elasticity. In the far field, the majority of off-fault aftershocks, including the M_w 5.7 aftershock on 13 August 2021, occurred in areas of increased CFS.

Figure 9b shows the coseismic Δ CFS on the surrounding faults (Table S3). The Maduo earthquake increased the CFS by ≥ 10 KPa on a number of faults, including the Maduo-Gande fault (MD-GD), the Jiangcuo fault (JC), and the Gander South Margin fault (GSM) west of the epicenter, and some segments of the Dari fault (DR) and the Bayan Kara Main Mountain fault (BKMM) south of the epicenter. The stress change on the East Kunlun fault (EKL) is minor, due to the greater distance. The results in Figure 9 are calculated using a friction coefficient of 0.4. We varied the coefficient in the range of 0.1–0.7. Using different friction coefficient values affect the calculated stress values, but the Δ CFS pattern in Figure 9a and the sign of stress changes (increase/decrease) in Figure 9b remain largely the same (Fig. S5).

DISCUSSION

In this study, we jointly inverted InSAR and GPS measurements to constrain the fault source model of the 2021 Maduo earthquake and calculated its impact of stress changes on the regional faults.

Many aspects of the Maduo earthquake have been published based on limited geodetic and seismicity data, with a simplified fault model. Here, we explain the choice of our model parameter, compare our results with previous studies, and discuss the implications for regional crustal deformation and seismicity.

Fault dip angles

In **Fault Source Model** section, we discussed our choice of the parameters of the fault source model, the optimization of the values of these parameters, and the associated uncertainties. One major assumption we made was a constant dip for F1 and F2, respectively. This is clearly a simplification; here, we show why this assumption is reasonable.

For a pure strike-slip event, the directionality and magnitude of the surface motion across the rupture can shed light

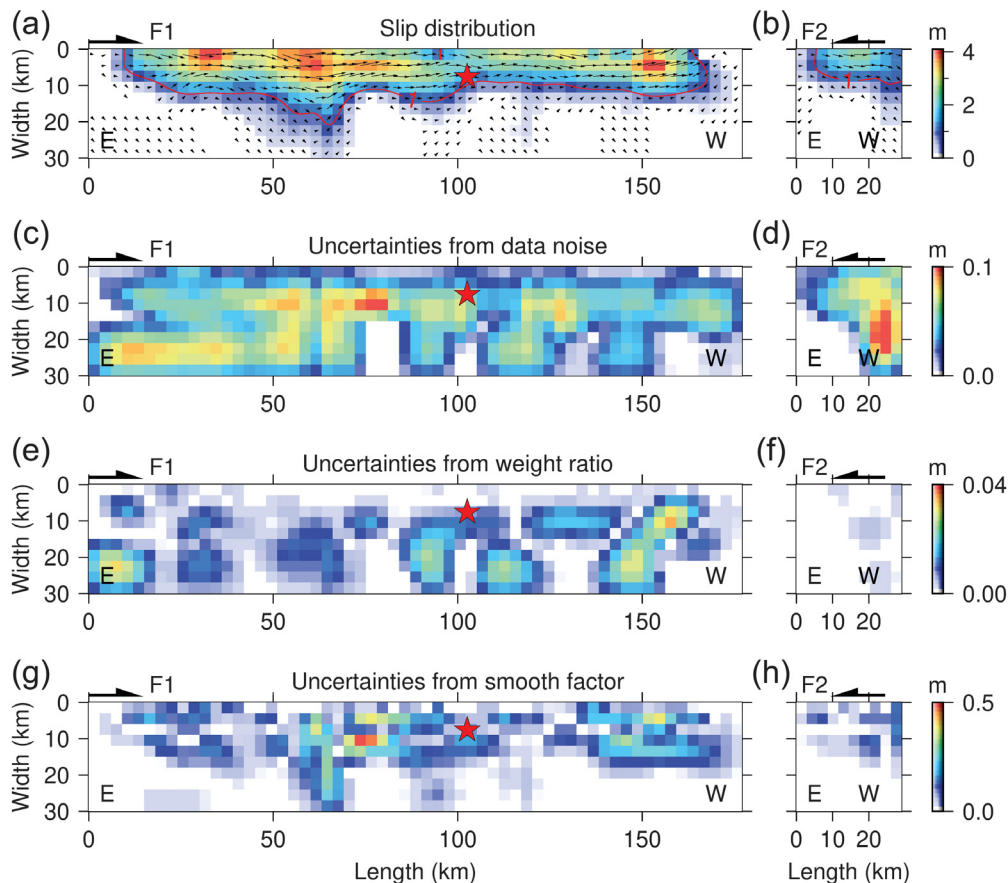


Figure 6. Fault-slip distribution and its uncertainties in a 2D projection. (a,b) Fault slip on the main fault F1 and the minor fault F2, respectively. (c,d) Corresponding uncertainties of slip (a) and (b) as a result of data noises, respectively. (e,f) Similar to (c,d), but for the uncertainties from weight ratio of GPS to InSAR data. (g,h) Similar to (c, d), but for uncertainties from smoothing factor. Red contour line in (a,b) represents 1 m slip. Black arrows indicate the magnitude and azimuth of sliding in fault patches. The red star is the mainshock from Wang *et al.* (2021).

on the fault dip angle (Jolivet *et al.*, 2014). According to the elastic dislocation model (Okada, 1985), the ratio of the maximum surface motion on both sides of a pure strike-slip fault is determined by the dip angle. For a vertical fault, this ratio is -1 , that is, opposite motion directions with the same magnitude. Therefore, the fault-perpendicular profiles of surface deformation can reveal the characteristics of the dip angle change (Jolivet *et al.*, 2014).

We used the deformation fields in east–west and north–south direction resolved by Liu *et al.* (2021) to synthesize the horizontal deformation fields (Fig. S1a). Five fault-perpendicular profiles of surface motions across F1 were shown in Figure S1b, and the ratios of the extreme horizontal motion on both sides of the fault were calculated. These ratios are close (within -1.17 to -1.35), which means similar fault dip angles along the fault strike (Jolivet *et al.*, 2014). According to theoretical simulation, the corresponding dip angle is 77.5° – 82.5° (Fig. S1c), with less than 5° along-strike variation. Such a small change of dip angle is difficult to distinguish

by the InSAR data and/or relocated aftershocks. Therefore, we chose to use a single dip angle for F1 and F2, respectively. In addition, all the ratios are smaller than -1.0 , indicating that the magnitude of the horizontal movements north of the rupture is greater than those in the south, which is more consistent with a steep north-dipping fault model than a vertical (Liu *et al.*, 2021) or a south-dipping one (segment 1 in Zhao *et al.*, 2021).

Comparison with previous fault source model and CFS change

Our optimal fault model includes a main rupture F1 and a secondary rupture F2 (Fig. 5). Whereas the strike of F1 is similar to previous studies, the optimal dip angle of F1 (78°) is larger than that (64.4°) constrained by the GPS data alone (Li Z. *et al.*, 2021) and smaller than that (90°) derived by the 3D deformation data based on InSAR alone (Liu *et al.*, 2021) (Table 1). The secondary rupture F2 is determined by the pixel offsets; this minor rupture

was not resolved in previous studies (Wang *et al.*, 2021; Li, Ding, *et al.*, 2021). Chen *et al.* (2021) and Zhao *et al.* (2021) suggested a five-segment planar fault model with five dip angles based on InSAR data, assuming that the near-rupture displacements are only caused by the corresponding fault segment, which differs from other studies and our nonplanar fault model (Table 1). He *et al.* (2021) recently suggested a nonplanar fault model with variable dip angles, inferred from the relocated aftershocks. From the fault-perpendicular profiles of surface deformation (Fig. S1), we found that the along-strike variation of the dip angle is small and chose to use a single optimal dip angle for F1 and F2, respectively.

Our slip-distribution model indicates that most slip occurred in the depth range of 0–15 km (Fig. 5), deeper than 0–5 km resolved from GPS data alone (Li, Ding, *et al.*, 2021) and similar to that derived by InSAR inversion (Chen *et al.*, 2021; He *et al.*, 2021; Liu *et al.*, 2021; Zhao *et al.*, 2021). The slip distribution resolved by sparse GPS data (Li, Ding, *et al.*, 2021) lacks the resolution and differs significantly from those

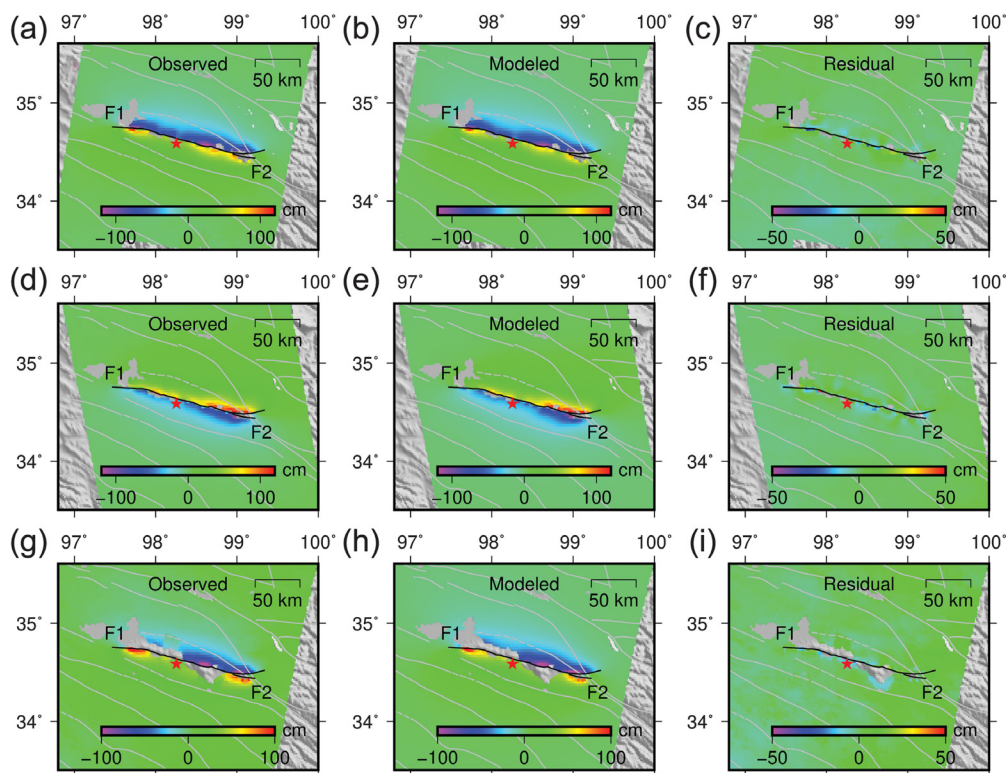


Figure 7. Comparison of observed and modeled InSAR displacement for the optimal fault-source model. (a–c) Observed, predicted, and residual displacement for the S1D measurement, respectively, (d–f) same as (a–c) but for the S1A measurement, (g–i) same as (a–c) but for the A2D measurement. The root mean square error (RMSE) is 4.8 cm for S1D, 4.7 cm for S1A, and 4.9 cm for A2D.

derived from InSAR measurement (Chen *et al.*, 2021; He *et al.*, 2021; Liu *et al.*, 2021; Zhao *et al.*, 2021) and our joint InSAR and GPS inversion (Fig. 5). The nearly horizontal slip in the fault patches (Fig. 6a,b) differs from significant dipping slip in the segmented fault model (Zhao *et al.*, 2021) and the finite-fault solution from USGS (see [Data and Resources](#)). Finally, the moment release calculated in this study (1.65×10^{20} N · m) is slightly less than the estimate (1.85×10^{20} N · m) from GPS data alone (Li, Ding, *et al.*, 2021) but falls between those (1.45×10^{20} N · m $\sim 1.8 \times 10^{20}$ N · m) derived from InSAR and/or aftershocks data (Chen *et al.*, 2021; He *et al.*, 2021; Liu *et al.*, 2021).

Differences in fault source models also affect the Δ CFS calculations. Li, Huang, *et al.* (2021) suggested significant coseismic CFS increases in the Maqin–Maqu segment and the middle segment of the YS-GZ fault. In contrast, our results, using the same friction coefficient, indicate minor (<10 KPa) Δ CFS on these distant faults (Fig. 9b). Only when we considered the contribution of postseismic stress change due to viscoelastic relaxation for 50 yr do we see >10 KPa stress increase on the YS-GZ fault (Fig. S6). Our coseismic Δ CFS for the optimal planes of the mainshock (Fig. 9a) is comparable to that from He *et al.* (2021), with some discrepancies near the rupture.

Discrepancy between geodetic inversion and field measurement

Our optimal model for coseismic slip (Figs. 5, 6a,b) indicates rupture to the ground surface in most places along the rupture zone, generally consistent with field studies (Li Z.-M. *et al.*, 2021). However, there are some noticeable differences. For example, our model suggests that coseismic slip in some of the shallowest patches can reach 3–4 m (Figs. 5, 6a–b), generally consistent with the surface displacement from SAR data (Fig. S1) and the previous source models (Chen *et al.*, 2021; He *et al.*, 2021; Li, Ding, *et al.*, 2021), but exceeds the field measurement of 1–2 m (Li Z.-M. *et al.*, 2021). Although the fault-slip model has more shallow patches with conspicuous slip (>3 m) east of the epicenter than in the west (Figs. 5, 6a), field investigation suggested a clearer rupture in

the western segment (Li Z.-M. *et al.*, 2021). One explanation for these discrepancies is that the surface is overlaid by a soft sedimentary layer, making it difficult to record the dislocation entirely through geomorphological markers. The Unmanned Aerial Vehicle imaging and onsite surveys (Fig. S7) show that there are thick loose sediments and abundant water sources in the rupture zone. The loose and watery sediments could make the surface rupture more diffuse and more complex (Li Z.-M. *et al.*, 2021). Moreover, the elastic dislocation theory used in the model does not apply to loose sediments.

Crustal deformation and seismicity of the Bayan Har block

The 2021 Maduo earthquake provides some useful insights into present-day crustal deformation in the Tibetan plateau. The broad and diffuse crustal deformation in the Tibetan plateau (and other regions of continental deformation) has been described by two end-member models. One model describes the Tibetan deformation as rigid blocks (or microplates) moving coherently along their strike-slip boundary faults (Avouac and Tapponnier, 1993; Replumaz and Tapponnier, 2003). The other model views the deformation field as being continuous similar to viscous flow (England and Molnar, 1997; Yang and Liu, 2009). These two end-member views have not been distinguished by the

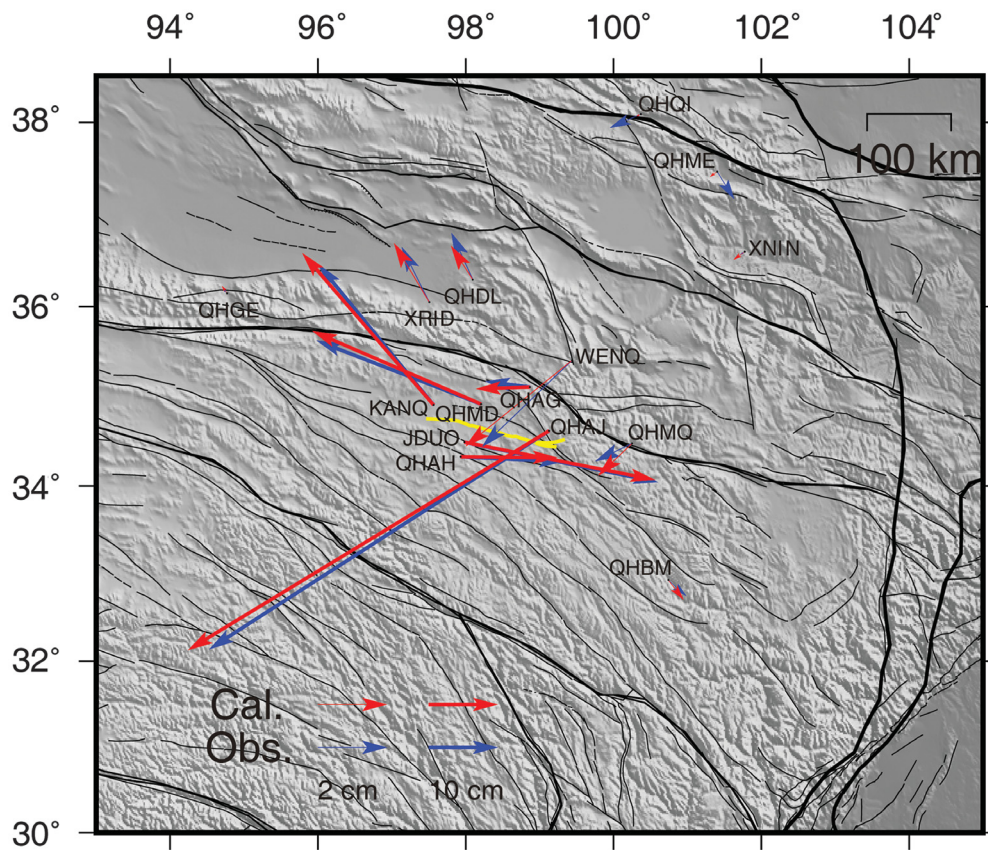


Figure 8. Comparison of observed and modeled GPS horizontal displacement for the optimal fault-source model. The RMSE of the east and north deformation is 8 mm and 5 mm, respectively. The yellow line is the fault trace in surface.

GPS data, which have been interpreted by both discrete block models (Shen *et al.*, 2005; Li *et al.*, 2018) and continuous deformation models (Zhang *et al.*, 2004). Others have tried to reconcile the different views with models that have multiscale quasi-rigid blocks and noticeable intrablock deformation (Thatcher, 2007; Loveless and Meade, 2011).

The Bayan Har block, bounded by the sinistral East Kunlun fault to the north and the Yushu–Ganze–Xianshuihe fault to the south (Fig. 1), is generally viewed as a major block extruding eastward along these two boundary faults. The Maduo earthquake, as well as numerous large earthquakes in the surrounding region (Fig. 9), illustrates important internal deformation within the Bayan Har block. The largest event, the 1947 M 7.75 Dari earthquake, produced an \sim 70-km-long rupture with 2–4 m left-lateral slip (Liang *et al.*, 2014, 2020) to the southeast of the Maduo rupture (Fig. 9). Xiong *et al.* (2010) reported an approximately 50-km-long late Quaternary rupture of the Gande segment of the Maduo–Gande fault, with maximum left-lateral and vertical dislocations of \sim 7.6 m and \sim 4 m, respectively. These intrablock earthquakes indicate that the Bayan Har is not a rigid block. Because the Maduo fault and the other intrablock seismogenic faults are predominately sinistral strike-slip faults

subparallel to the East Kunlun fault (Fig. 9), one may also view the deformation as being accommodated by diffuse block boundary fault zones rather than a single boundary fault.

Nonetheless, the intrablock seismicity is much weaker than that on the block boundary faults (Fig. 1). No strong earthquakes ($M_w \geq 6$) have been recorded in the intrablock faults or fault segments where the CFS was increased more than 10 KPa by the Maduo earthquake (Fig. 9b). Whether such stress increase has significant impact on future seismicity on these faults is difficult to assess, because of the lack of stress history information and sufficiently complete earthquake catalogs. The Maduo event itself was probably delayed by both a history of strong earthquakes around the Bayan Har block (Dong *et al.*, 2021) and the three strong earthquakes nearby (Fig. S8); these events lowered the CFS on the Maduo rupture zone.

We also calculated the Δ CFS caused by postseismic viscoelastic relaxation (Fig. S6). In 50 yr, the postseismic process of the Maduo earthquake will increase the CFS by more than 10 KPa on the Maqin segment (longitude $100^\circ\sim 101^\circ$ E), the west segment (longitude $96^\circ\sim 97^\circ$ E) of the East Kunlun fault, and the eastern segment of the Yushu–Ganze fault (longitude $97^\circ\sim 98^\circ$). These fault segments have high slip rates and potential for producing large earthquakes. Particularly, the Maqin segment is a seismic gap, and it has seen an increase of CFS from the historical earthquakes (Fig. S8 and Dong *et al.*, 2021) and the Maduo event (Fig. S6).

CONCLUSIONS

We have jointly inverted InSAR data and GPS data to constrain the geometry of the ruptured fault plane and coseismic slip of the 2021 Maduo earthquake. Our optimal fault source model includes a \sim 156 km northwest-striking main fault plane that dips 78° , and a \sim 24 km secondary fault plane with southeast-striking and 64° dipping. The along-strike variation of the dipping angle of the main rupture plane is less than 5° . Most coseismic slip occurred in the depth of 0–15 km, in which slip is more than 1 m. The slip vectors are nearly horizontal

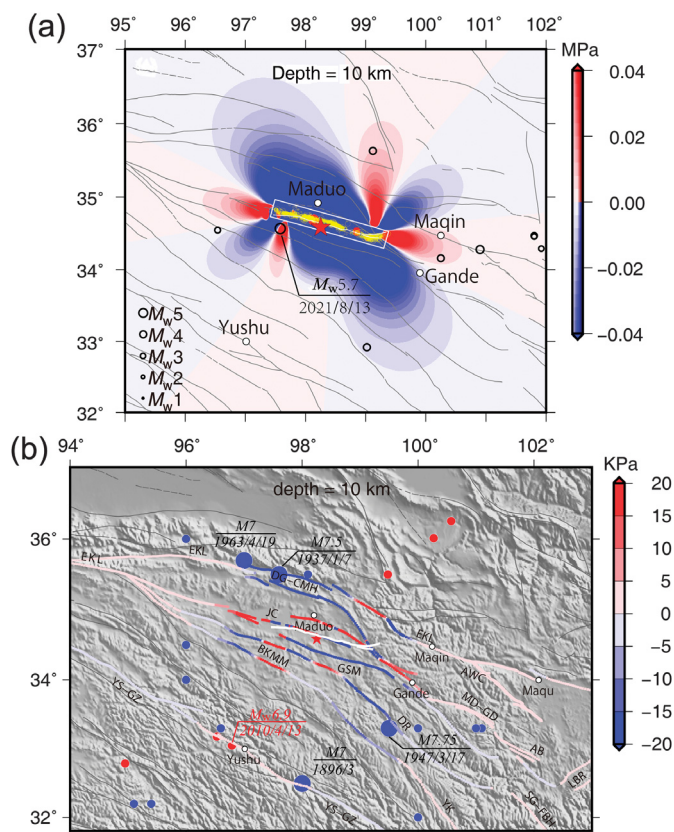


Figure 9. Coseismic Coulomb failure stress changes due to the Maduo earthquake. (a) Stress change at the depth of 10 km, calculated by assuming the receiving fault parameters are the same as those of the mainshock rupture (strike = 282°, dip = 78°, rake = -1.3°, friction = 0.4). The near-field relocated aftershocks within the depth of 5–15 km, one month after the mainshock, are denoted by yellow dots (Wang *et al.*, 2021). The far-field unrelocated earthquakes from CENC within the depth of 0–20 km, two months after the mainshock, are denoted by black circles. The white rectangle is the schematic vicinity area, where the calculated stress change may be unreliable because linear elasticity may not apply there. (b) Stress change on the surrounding faults, at 10 km depth (friction = 0.4). The blue solid circles are $M \geq 6$ earthquakes before 1976 (from CENC). The red solid circles are $M_w \geq 6$ earthquakes since 1976 (from Global CMT). The white line is the rupture zone of the Maduo earthquake. The parameters of receiver faults are in Table S3. Abbreviations for the fault: AB, the A Bar fault; AWC, the A Wancang fault; BKMM, the Bayan Kara Main Mountain fault; DG-CMH, the Dagou–Changmahe fault; DR, the Dari fault; EKL, the East Kunlun fault; GSM, the Gander South Margin fault; JC, the Jianguo fault; LRB, the Longriba fault; MD-GD, the Maduo–Gander fault; SG-FBH, the Songgang–Fubianhe fault; YK, the Yuke fault; YS-GZ, the Yushu–Ganzi fault. The faults are from Xu *et al.* (2016) and Deng *et al.* (2003).

everywhere, indicating a nearly pure sinistral strike-slip event. The seismic moment derived from this slip-distribution model is about 1.65×10^{20} N·m, equivalent to a moment magnitude of M_w 7.42 and slightly larger than that derived from the focal mechanism solutions. The vicinity aftershocks occurred mainly near the fault plane where coseismic slip was low. The Maduo earthquake increased the CFS more than 10 KPa on the surrounding faults, but the impact on seismic hazard on these faults

is difficult to assess because of the incomplete catalog and uncertainty of stress history on these faults. Our calculated stress perturbation on the more distant East Kunlun fault and Yushu–Ganze fault is less than previously reported. The 2021 Maduo earthquake, and some of the previous earthquakes in this region, indicate noticeable internal deformation of the Bayan Har block. Thus, the Bayan Har block cannot be treated as a rigid block, and the deformation is accommodated by diffuse block boundary fault zones rather than single boundary faults.

DATA AND RESOURCES

The Sentinel-1 SLC data were provided by the European Space Agency (ESA) and downloaded from the Alaska Satellite Facility (<https://www.asf.alaska.edu/>, last accessed August 2021). The Advanced Land Observation Satellite-2 (ALOS-2) ScanSAR SLC data were provided by the Japan Aerospace Exploration Agency (JAXA). The Global Centroid Moment Tensor (Global CMT) earthquake catalog was from <https://www.globalcmt.org/CMTsearch.html> (last accessed September 2021). The U.S. Geological Survey (USGS) earthquake catalog was searched from <https://earthquake.usgs.gov/earthquakes/search> (last accessed September 2021). The German Research Centre for Geosciences (GFZ) earthquake catalog was from <https://geofon.gfz-potsdam.de> (last accessed September 2021). The China Earthquake Networks Center (CENC) earthquake catalog was provided by the CENC, National Earthquake Data Center (<https://data.earthquake.cn/>, last accessed September 2021) (user registration is required). The down-sampled Interferometric Synthetic Aperture Radar (InSAR) coseismic displacement data and the retrieved fault-slip distribution by this study is uploaded to <https://doi.org/10.6084/m9.figshare.16441890.v1> (last accessed February 2022). The Global Positioning System (GPS), relocated aftershocks, and horizontal deformation fields are from the corresponding references that have been published. The supplemental material for this article includes two text files, eight figures, and four tables.

DECLARATION OF COMPETING INTERESTS

The authors acknowledge that there are no conflicts of interest recorded.

ACKNOWLEDGMENTS

The authors thank the two anonymous reviewers and the Associate Editor Ronni Grapenthin for constructive comments and suggestions. This study is supported by the Basic Research program from the Institute of Earthquake Forecasting, China Earthquake Administration (Grant Number 2018IEF010103), the high-resolution seismic monitoring and emergency application program (31-Y30F09-9001-20/22), and the National Key R&D Program of China (Grant Number 2017YFB0502700) to Hong, the National Natural Science Foundation of China (41874024) and National Key R&D Program of China (2019YFE0108900) to Meng. Most of the figures were generated with the Generic Mapping Tools (GMT). The authors thank Xin Zhou from National Institute of Natural Hazards for providing the elastic dislocation code.

REFERENCES

Avouac, J.-P., and P. Tapponnier (1993). Kinematic model of active deformation in Central Asia, *Geophys. Res. Lett.* **20**, 895–898.

- Bassin, C., G. Laske, and G. Masters (2000). The current limits of resolution for surface wave tomography in North America, *Eos Trans. AGU* **81**, Fall Meet. Suppl. Abstract, F897.
- Casu, F., A. Manconi, A. Pepe, and R. Lanari (2011). Deformation time-series generation in areas characterized by large displacement dynamics: The SAR amplitude pixel-offset SBAS technique, *IEEE Trans. Geosci. Remote Sens.* **49**, 2752–2763.
- Chen, H., C. Qu, D. Zhao, C. Ma, and X. Shan (2021). Rupture kinematics and coseismic slip model of the 2021 M_w 7.3 Maduo (China) earthquake: Implications for the seismic hazard of the Kunlun fault, *Remote Sens.* **13**, 3327, doi: [10.3390/rs13163327](https://doi.org/10.3390/rs13163327).
- Deng, Q., P. Zhang, Y. Ran, X. Yang, W. Min, and Q. Chu (2003). Basic characteristics of active tectonics of China, *Sci. China Ser. D* **46**, 356–372 (in Chinese).
- Deng, Q. D., X. Gao, G. H. Chen, and H. Yang (2010). Recent tectonic activity of Bayankala fault-block and the Kunlun-Wenchuan earthquake series of the Tibetan Plateau, *Earth Sci. Front.* **17**, 163–178 (in Chinese).
- Dong, P., B. Zhao, and X. Qiao (2021). Interaction between historical earthquake and the 2021 M_w 7.4 Maduo event and their impacts on the seismic gap areas along the East Kunlun Fault, *Earth Planets Space* doi: [10.21203/rs.3.rs-934288/v1](https://doi.org/10.21203/rs.3.rs-934288/v1).
- England, P., and P. Molnar (1997). Active deformation of Asia: From kinematics to dynamics, *Science* **278**, 647–650.
- Farr, T. G., P. A. Rosen, E. Caro, R. Crippen, R. Duren, S. Hensley, M. Kobrick, M. Paller, E. Rodriguez, L. Roth, *et al.* (2007). The shuttle radar topography mission, *Rev. Geophys.* **45**, RG2004, doi: [10.1029/2005RG000183](https://doi.org/10.1029/2005RG000183).
- Feng, W. P., and Z. H. Li (2010). A novel hybrid PSO/simplex algorithm for determining earthquake source parameters using InSAR data, *Prog. Geophys.* **25**, 1189–1196 (in Chinese).
- Gardner, A. S., G. Moholdt, T. Scambos, M. Fahnestock, S. Ligtenberg, M. van den Broeke, and J. Nilsson (2018). Increased West Antarctic and unchanged East Antarctic ice discharge over the last 7 years, *Cryosphere* **12**, 521–547.
- Goldstein, R. M., H. A. Zebker, and C. L. Werner (1988). Satellite radar interferometry: Two-dimensional phase unwrapping, *Radio Sci.* **23**, 713–720.
- Gray, A. L., K. E. Mattar, and G. Sofko (2000). Influence of ionospheric electron density fluctuations on satellite radar interferometry, *Geophys. Res. Lett.* **27**, 1451–1454.
- He, K., Y. Wen, C. Xu, and Y. Zhao (2021). Fault geometry and slip distribution of the 2021 M_w 7.4 Maduo, China, earthquake inferred from InSAR measurements and relocated aftershocks, *Seismol. Res. Lett.* **93**, 8–20.
- Jolivet, R., Z. Duputel, B. Riel, M. Simons, L. Rivera, S. E. Minson, H. Zhang, M. A. G. Aivazis, F. Ayoub, *et al.* (2014). The 2013 M_w 7.7 Balochistan earthquake: Seismic potential of an accretionary wedge, *Bull. Seismol. Soc. Am.* **104**, 1020–1030.
- Jones, L. M., W. Han, E. Hauksson, A. Jin, Y. Zhang, and Z. Luo (1984). Focal mechanisms and aftershock locations of the Songpan earthquakes of August 1976 in Sichuan, China, *J. Geophys. Res.* **89**, 7697–7707.
- Jónsson, S., H. Zebker, P. Segall, and F. Amelung (2002). Fault slip distribution of the 1999 M_w 7.1 Hector Mine, California, earthquake, estimated from satellite radar and GPS measurements, *Bull. Seismol. Soc. Am.* **92**, 1377–1389, doi: [10.1785/0120000922](https://doi.org/10.1785/0120000922).
- Lasserre, C., G. Peltzer, F. Crampé, Y. Klinger, J. Van der Woerd, and P. Tapponnier (2005). Coseismic deformation of the 2001 M_w = 7.8 Kokoxili earthquake in Tibet, measured by synthetic aperture radar interferometry, *J. Geophys. Res.* **110**, no. B12, doi: [10.1029/2004JB003500](https://doi.org/10.1029/2004JB003500).
- Lei, Y., A. Gardner, and P. Agram (2021). Autonomous repeat image feature tracking (autoRIFT) and its application for tracking ice displacement, *Remote Sens.* **13**, 749, doi: [10.3390/rs13040749](https://doi.org/10.3390/rs13040749).
- Li, Y., L. Huang, R. Ding, S. Yang, L. Liu, S. Zhang, and H. Liu (2021). Coulomb stress changes associated with the $M_{7.3}$ Maduo earthquake and implications for seismic hazards, *Nat. Hazards Res.* **1**, 95–101.
- Li, Y., M. Liu, Q. Wang, and D. Cui (2018). Present-day crustal deformation and strain transfer in northeastern Tibetan Plateau, *Earth Planet. Sci. Lett.* **487**, 179–189.
- Li, Z., K. Ding, P. Zhang, Y. Wen, L. Zhao, and J. Chen (2021). Coseismic deformation and slip distribution of 2021 M_w 7.4 Madoi earthquake from GNSS observation, *Geomat. Inf. Sci. Wuhan Univ.* **46**, 1489–1497, doi: [10.13203/j.whugis20210301](https://doi.org/10.13203/j.whugis20210301) (in Chinese).
- Li, Z., J. R. Elliott, W. Feng, J. A. Jackson, B. E. Parsons, and R. J. Walters (2011). The 2010 M_w 6.8 Yushu (Qinghai, China) earthquake: Constraints provided by InSAR and body wave seismology, *J. Geophys. Res.* **116**, no. B10, doi: [10.1029/2011JB008358](https://doi.org/10.1029/2011JB008358).
- Li, Z.-M., W.-Q. Li, T. Li, Y.-R. Xu, P. Su, G. Peng, H.-Y. Sun, G.-H. Ha, G.-H. Chen, and Z.-D. Yuan (2021). Seismogenic fault and coseismic surface deformation of the Maduo M_s 7.4 earthquake in Qinghai, China: A quick report, *Seismol. Geol.* **43**, 722–737 (in Chinese).
- Liang, C., and E. J. Fielding (2017). Measuring azimuth deformation with L-band ALOS-2 ScanSAR interferometry, *IEEE Trans. Geosci. Remote Sens.* **55**, 2725–2738.
- Liang, C., Z. Liu, E. J. Fielding, and R. Bürgmann (2018). InSAR time series analysis of L-band wide-swath SAR data acquired by ALOS-2, *IEEE Trans. Geosci. Remote Sens.* **56**, 4492–4506.
- Liang, M.-J., Y. Yang, F. Du, Y. Gong, W. Sun, M. Zhao, and Q. He (2020). Late quaternary activity of the central segment of the Dari fault and restudy of the surface rupture zone of the 1947 $M_{7.3/4}$ Dari earthquake, Qinghai province, *Seismol. Geol.* **42**, 703–714 (in Chinese).
- Liang, M.-J., R.-J. Zhou, L. Yan, G.-H. Zhao, and H.-M. Guo (2014). The relationships between neotectonics activity of the middle segment of Dari fault and its geomorphological response, Qinghai province, China, *Seismol. Geol.* **36**, 28–38 (in Chinese).
- Liu, J., J. Hu, Z. Li, Z. Ma, L. Wu, W. Jiang, G. Feng, and J. Zhu (2021). Complete three-dimensional coseismic displacements due to the 2021 Maduo earthquake in Qinghai Province, China from Sentinel-1 and ALOS-2 SAR images, *Sci. China Earth Sci.* doi: [10.1007/s11430-021-9868-9](https://doi.org/10.1007/s11430-021-9868-9).
- Loveless, J., and B. Meade (2011). Partitioning of localized and diffuse deformation in the Tibetan Plateau from joint inversions of geologic and geodetic observations, *Earth Planet. Sci. Lett.* **303**, 11–24.
- Marius, I., S. Henriette, H. Sebastian, S. Andreas, D. Simon, and V.-B. Hannes (2017). Kite—Software for rapid earthquake source optimisation from InSAR surface displacement, *GFZ Data Serv.* doi: [10.5880/GFZ.2.1.2017.002](https://doi.org/10.5880/GFZ.2.1.2017.002).
- Okada, Y. (1985). Surface deformation due to shear and tensile faults in a half-space, *Bull. Seismol. Soc. Am.* **75**, 1135–1154.

- Parsons, B., T. Wright, P. Rowe, J. Andrews, J. Jackson, R. Walker, M. Khatib, M. Talebian, E. Bergman, and E. R. Engdahl (2006). The 1994 Sefidabeh (eastern Iran) earthquakes revisited: New evidence from satellite radar interferometry and carbonate dating about the growth of an active fold above a blind thrust fault, *Geophys. J. Int.* **164**, 202–217.
- Replumaz, A., and P. Tapponnier (2003). Reconstruction of the deformed collision zone between India and Asia by backward motion of lithospheric blocks, *J. Geophys. Res.* **108**, no. B6, doi: [10.1029/2001JB000661](https://doi.org/10.1029/2001JB000661).
- Rosen, P. A., E. Gurrola, G. F. Sacco, and H. Zebker (2012). The InSAR scientific computing environment, *EUSAR 2012, 9th European Conf. Synthetic Aperture Radar*, Nuremberg, Germany, 23–26 April 2012, 730–733.
- Shen, Z.-K., J. Lü, M. Wang, and R. Bürgmann (2005). Contemporary crustal deformation around the southeast borderland of the Tibetan Plateau, *J. Geophys. Res.* **110**, no. B11, doi: [10.1029/2004JB003421](https://doi.org/10.1029/2004JB003421).
- Shen, Z.-K., J. Sun, P. Zhang, Y. Wan, M. Wang, R. Bürgmann, Y. Zeng, W. Gan, H. Liao, and Q. Wang (2009). Slip maxima at fault junctions and rupturing of barriers during the 2008 Wenchuan earthquake, *Nat. Geosci.* **2**, 718–724.
- Thatcher, W. (2007). Microplate model for the present-day deformation of Tibet, *J. Geophys. Res.* **112**, no. B1, doi: [10.1029/2005JB004244](https://doi.org/10.1029/2005JB004244).
- Wang, R., F. Diao, and A. Hoehner (2013). SDM—A geodetic inversion code incorporating with layered crust structure and curved fault geometry, *EGU General Assembly 2013*, Vienna, Austria, 7–12 April 2013, EGU2013-2411-1.
- Wang, R., F. Lorenzo-Martín, and F. Roth (2006). PSGRN/PSCMP—A new code for calculating co- and post-seismic deformation, geoid and gravity changes based on the viscoelastic-gravitational dislocation theory, *Comput. Geosci.* **32**, 527–541.
- Wang, W., L. Fang, J. Wu, H. Tu, L. Chen, G. Lai, and L. Zhang (2021). Aftershock sequence relocation of the 2021 M_s 7.4 Maduo earthquake, Qinghai, China, *Sci. China Earth Sci.* **64**, doi: [10.1007/s11430-021-9803-3](https://doi.org/10.1007/s11430-021-9803-3) (in Chinese).
- Wang, J., C. Xu, J. T. Freymueller, and Z. Li (2017). Probing Coulomb stress triggering effects for a $M_w > 6.0$ earthquake sequence from 1997 to 2014 along the periphery of the Bayan Har block on the Tibetan Plateau, *Tectonophysics* **694**, 249–267.
- Xiong, R.-W., J.-W. Ren, J.-L. Zhang, P.-X. Yang, Z.-M. Li, C.-Z. Hu, and C.-Y. Chen (2010). Late Quaternary active characteristics of the Gande segment in the Maduo-Gande fault zone, *Earthquake* **30**, 65–73 (in Chinese).
- Xu, X.-W., Z.-J. Han, X.-P. Yang, S.-M. Zhang, G.-H. Yu, B.-G. Zhou, F. Li, B.-Q. Ma, G.-H. Chen, and Y.-K. Ran (2016). *Seismotectonic Map in China and Its Adjacent Regions [M]*, Seismological Press, Beijing (in Chinese).
- Yang, Y., and M. Liu (2009). Crustal thickening and lateral extrusion during the Indo-Asian collision: A 3D viscous flow model, *Tectonophysics* **465**, 128–135.
- Yang, W., Z. Ding, J. Liu, J. Cheng, X. Zhang, P. Wu, and Q. Yao (2021). Velocity structure of the northeastern end of the Bayan Har block, China, and the seismogenic environment of the Jiuzhaigou and Songpan-Pingwu earthquakes: Inferences from double-difference tomography, *Bull. Seismol. Soc. Am.* **111**, 2195–2208.
- Zhang, G. M., H. S. Ma, H. Wang, and X. L. Wang (2005). Boundaries between active-tectonic blocks and strong earthquakes in the China mainland, *Chin. J. Geophys.* **48**, 602–610 (in Chinese).
- Zhang, P.-Z., Z. Shen, M. Wang, W. Gan, R. Burgmann, P. Molnar, Q. Wang, Z. Niu, J. Sun, J. Wu, *et al.* (2004). Continuous deformation of the Tibetan Plateau from global positioning system data, *Geology* **32**, 809–812.
- Zhao, D., C. Qu, H. Chen, X. Shan, X. Song, and W. Gong (2021). Tectonic and geometric control on fault kinematics of the 2021 M_w 7.3 Maduo (China) earthquake inferred from interseismic, coseismic, and postseismic InSAR observations, *Geophys. Res. Lett.* **48**, e2021GL095417, doi: [10.1029/2021GL095417](https://doi.org/10.1029/2021GL095417).

Manuscript received 8 September 2021

Published online 22 February 2022